Exploring the relative contribution of mineralogy and CPO to the seismic velocity anisotropy of evaporites

Liliana Vargas-Meleza[a,b,*], David Healy[a], Ian Alsop[a], Nicholas E. Timms[c]

[a] *Dept. of Geology & Petroleum Geology, University of Aberdeen, Aberdeen, AB24 3UE, UK*
[b] *Mexican Petroleum Institute, Eje Central Lázaro Cárdenas 156, Mexico City, 07763, Mexico*
[c] *Dept. of Applied Geology, Curtin University, GPO Box U1987, Perth, WA 6845, Australia*

We present the influence of mineralogy and microstructure on the seismic velocity anisotropy of evaporites. Bulk elastic properties and seismic velocities are calculated for a suite of 20 natural evaporite samples, which consist mainly of halite, anhydrite, and gypsum. They exhibit strong fabrics as a result of tectonic and diagenetic processes. Sample mineralogy and crystallographic preferred orientation (CPO) were obtained with the electron backscatter diffraction (EBSD) technique and the data used for seismic velocity calculations. Bulk seismic properties for polymineralic evaporites were evaluated with a rock recipe approach. Ultrasonic velocity measurements were also taken on cube shaped samples to assess the contribution of grain-scale shape preferred orientation (SPO) to the total seismic anisotropy. The sample results suggest that CPO is responsible for a significant fraction of the bulk seismic properties, in agreement with observations from previous studies. Results from the rock recipe indicate that increasing modal proportion of anhydrite grains can lead to a greater seismic anisotropy of a halite-dominated rock. Conversely, it can lead to a smaller seismic anisotropy degree of a gypsum-dominated rock until an estimated threshold proportion after which anisotropy increases again. The difference between the predicted anisotropy due to CPO and the anisotropy measured with ultrasonic velocities is attributed to the SPO and grain boundary effects in these evaporites.

Keywords: Elastic properties, seismic velocity anisotropy, CPO, fabric, evaporite

1. Introduction

Although the anisotropic elastic properties of evaporite crystals have long been acknowledged (Kupfer, 1989; Sun et al., 1991; Aptukov et al., 2010), potential interactions between them as contributors to the bulk seismic anisotropy of evaporite rocks are poorly documented. Halite is the dominant mineral in evaporite rock sequences. As such, the study of seismic properties of evaporites has mostly focused on pure crystalline halite (Raymer et al., 2000a,b). However, chlorides (e.g., halite, sylvite, carnallite), sulphates (e.g., anhydrite, gypsum, polyhalite) and carbonates (e.g., dolomite, calcite), are often found interlayered with halite or in

*Corresponding author. Tel: +447891462282
Email addresses: liliana.meleza@abdn.ac.uk (Liliana Vargas-Meleza), d.healy@abdn.ac.uk (David Healy), ian.alsop@abdn.ac.uk (Ian Alsop), N.Timms@curtin.edu.au (Nicholas E. Timms)

minor amounts as secondary phases or solid inclusions. Furthermore, evaporite crystals can align along preferential directions induced by either tectonic deformation or diagenetic processes. This can produce strong fabrics and induce bulk seismic velocity anisotropy (Raymer et al., 2000b,a; Hildyard et al., 2009; Trippetta et al., 2010).

Among the microstructural factors that cause seismic velocity anisotropy are crystallographic preferred orientation (CPO), shape preferred orientation (SPO), variation in mineral and grain distribution, aligned pores, cracks, and fractures, and thin layering (Wenk et al., 2004). In polycrystalline rocks, bulk seismic properties result from the combination of the individual anisotropic elastic properties, modal content and geometrical arrangement of grains of the individual mineral constituents. Standard averaging methods are commonly used to determine the azimuthal distribution of compressional and shear wave velocities (V_P and V_S) from averaged elastic properties, based on the availability of single-crystal elastic properties, the volume fraction of mineral constituents and their CPO (Mainprice and Humbert, 1994; Mainprice and Nicolas, 1989; Lloyd and Kendall, 2005). Electron backscatter diffraction (EBSD) technique is now the standard technique to quantify CPO accurately (Prior et al., 1999). This methodology has been extensively applied to determine seismic properties of a wide range of rock types and geological settings (Mainprice and Nicolas, 1989; Burlini and Kunze, 2000; Valcke et al., 2006; Tatham, 2008; Tatham et al., 2008; Healy et al., 2009; Lloyd et al., 2009; Dempsey et al., 2011; Lloyd et al., 2011b,a; Ward et al., 2012; Almqvist et al., 2013). Studies on sedimentary rocks that have used this methodology are fewer and include works in clastic rocks (e.g., Louis et al., 2005; Valcke et al., 2006), polycrystalline synthetic and natural halite (e.g., Sun et al., 1991; Raymer et al., 2000a,b; Urai et al., 2008; Desbois et al., 2010), and on polycrystalline anhydrite (e.g., Boeyens and Ichhram, 2002; Hildyard et al., 2009). Other works consider calcite mylonite and micaceous carbonates (e.g., Burlini and Kunze, 2000; Wenk et al., 2004); all of which have found that fabrics and elastic properties of individual minerals contribute to the seismic character of a rock.

In this study, we explore 1) the influence of CPO development in evaporites, 2) the effects of mineralogy, e.g., halite, anhydrite, and gypsum, and 3) the effects of extrinsic structural factors, such as initial porosity, open aligned cracks, and SPO, on the resulting seismic velocity anisotropy of natural and hypothetical polymineralic evaporites. We used a suite of natural evaporite samples of three main lithologies (halite-, anhydrite-, and gypsum-dominated) with strong fabrics, which were collected from a single diapiric province in Nova Scotia. Our objective is to identify and separate the controlling factors on the distribution of seismic velocities from both microstructural analysis on thin sections and ultrasonic tests on cube shaped samples of the same rock specimens. Our results provide insights into the microstructural factors controlling seismic velocities of polymineralic evaporites to better understand the relationship between intrinsic and extrinsic sources of these characteristics.

2. Location of study

A suite of 20 samples, consisting of evaporites rich in halite, anhydrite and gypsum, was collected from a single diapiric province in Nova Scotia, Canada (Fig. 1a). Here, salt diapirs are prominent under the Gulf of St. Lawrence, along the Hollow Fault and onshore in Cape Breton Island. These thick (c. 1 km) evaporitic deposits correspond to the lower Windsor Group, of Visean age. Such evaporites are believed to have migrated from depths of 4 km and today are found tens to hundreds of metres below the ground level and exposed along the western shores of Nova Scotia (Howie, 1986).

[Figure 1 about here.]

Exposures of salt diapirs occur in continuous across-strike cliff sections, and have been previously documented by Alsop et al. (2000). They consist predominantly of gypsum mylonite and comprise the Broad Cove diapir (BC), Coal Mine Point diapir (CMP), Finlay Point diapir (FP) and Port Hood diapir (PH), (Fig. 1a). Outcrops are characterised by steep salt-siliciclastic contacts and a wide variety of fabrics that steepen progressively towards the subvertical diapiric contacts. As an example, the CMP salt diapir is shown in Fig. 1b-c, which exhibits strong deformation, distinctive foliation and fracturing. Several samples were taken to study a variety of fabrics within the same outcrop Fig. 1b-c. Additionally, several samples were taken from the Pugwash salt mine (PM), which contains strongly deformed, interlayered deposits of halite and anhydrite.

3. Sample description and preparation

Both the FP and PH salt diapir outcrops preserve fabrics and are characterised by light grey to orange, highly folded and strongly deformed bands of nodular gypsum, interlayered with thin clay seams (Fig. 2a-c). The BC diapir outcrop is characterised by distinctive lozenges of weakly deformed, bitumen-stained gypsum (Fig. 2d-e). The strongest foliation and deformation were observed at the CMP outcrop where a tightly folded mylonitic fabric, parallel to the diapiric margin, is cross-cut by strongly deformed, thin gypsum veins (Fig. 2f). Gypsum mylonites from the CMP outcrop are generally medium to dark grey, are denser than the other gypsum samples, and are interpreted to have larger anhydrite content (Table 1). In total, fifteen gypsum mylonite samples were obtained from these four outcrops.

Three halite samples were collected at PM. Two samples comprise >95 %, coarse-grained (2-10 mm grain size), milky white and reddish halite, and show grain shape preferred alignment visible at hand-sample scale (Fig. 2g). The third one is a colourless, single crystal of halite, of $6 \times 4 \times 3.5$ cm dimensions. Additionally, two anhydrite samples from PM are dark-grey, dense, fine-grained and exhibit visible traces of laminations (Fig. 2h).

[Figure 2 about here.]

All 20 samples for ultrasonic tests (listed in Table 1) were cut dry into cuboids from larger blocks and oriented with respect to the foliation visible on the specimens (i.e., the foliation is parallel to two of the cut faces). The convention for the orthogonal reference axes in the sample reference frame is defined such that X direction is oriented parallel to the lineation; X-Y is the foliation plane; and Z direction is normal to the foliation plane (Fig. 2i). The cut surfaces were polished to facilitate coupling with the velocity measurement apparatus. The dimensions of each sample were precisely measured with an electronic caliper, which range from 4 cm to 6.5 cm face length. Dry density (ρ) for each sample was calculated by determining mass (M) and bulk volume (V), which is defined as $\rho = M/V$. These properties were determined at atmospheric pressure and temperature conditions. Slabs of 50×25 mm with a thickness of 30 mm were cut perpendicular to the foliation plane (i.e., parallel to the X-Z plane) for a subset of five selected samples: two fine-grained anhydrite samples (PMDH02, PMDH03), two coarse-grained halite samples (PMDH01, PMDH04) and one gypsum mylonite sample (BCDH02). Thin sections were prepared with a standard thickness of 30 μm.

3.1. EBSD settings

Prior to EBSD analysis, the anhydrite and gypsum mylonite thin sections were polished with 0.6 μm colloidal silica in hydroxide using a Vibromet II polisher, then a thin carbon coat was applied. Due to the high solubility of halite, the final polish of the halite samples involved gently wiping with a damp lint-free tissue, dried, and left uncoated. Consequently, the minor anhydrite grains present in these samples were not polished sufficiently to yield EBSD data.

4. Methods

The method used in this study to calculate the bulk seismic properties requires: 1) the measurement of crystallographic orientations of minerals in a polished thin section, 2) the elastic stiffness coefficients and density of the single crystals of each mineral constituent, and 3) the modal content of each mineral phase. Firstly, crystallographic orientations are measured using standard electron backscattered diffraction (EBSD) technique (Prior et al., 1999). Secondly, once the CPO has been determined, the bulk elastic stiffness matrix is obtained by modulating the individual elastic properties proportionally to the modal content and rotating it according to the CPO of each mineral. Then, the bulk seismic properties can be determined from the bulk elastic properties (Mainprice and Humbert, 1994). Finally, bench-top ultrasonic velocity measurements were taken on the cube shaped samples. Details on each step of our methodology are present below.

4.1. CPO determination

EBSD data were collected on a Zeiss EVO W-filament SEM and a Zeiss NEON40 dual beam FIB-FEG-SEM at Curtin University, Western Australia, both fitted with Oxford Instruments Channel 5 EBSD acquisition system and Nordlys 2 EBSD cameras. SEM operating conditions were routine for EBSD analysis (20 kV acceleration voltage, 70° sample tilt, 15 mm working distance, and spot size 550 on the EVO),

(Prior et al., 1999). Match units for anhydrite were developed from crystallographic data of Hawthorne and Ferguson (1975) transformed from space group Amma (which uses c a b coordinate system) to Cmcm (which uses standard Mermann-Mauguin a b c coordinate system used by Channel 5 EBSD software). Match units for gypsum were developed from crystallographic data of Boeyens and Ichhram (2002) with space group C2/c. Full details of the crystallographic parameters for anhydrite and gypsum are given by (Hildyard et al., 2009, Table 3). These match units were developed with 60 reflectors. The default halite match units supplied in the Channel 5 HKL phase database were utilised to index halite.

Maps were collected over areas sufficiently large to sample a statistically representative number of grains, with step sizes small enough to collect several points per grain. Thus, to adequately characterise the halite with large grain sizes, stitching of multiple individual maps was required. Angular mismatches at the stitched map borders associated with changes in the beam-sample geometry over wide areas were mostly corrected for in the software. However, some such artefacts remain. Gypsum damages rapidly under the electron beam such that EBSD patterns completely disappeared after ∼1 s (Hildyard et al., 2009). Therefore, EBSD acquisition settings in Channel 5 Flamenco was optimised for rapid data acquisition per point, which included 40 ms pattern acquisition time, 64 frame background subtraction, 4×4 binning, Hough resolution of 65. This resulted in a mapping rate of 0.165 s per point.

For anhydrite, indexing rate was improved from ∼35 % to ∼60 % by using 4-6 bands (instead of 6-8 bands) and band centres. However, some grains with high band contrast remained un-indexed and a very minor proportion of misindexing occurred. Indexing of gypsum used 4-7 bands and band centres. However, some grains with high band contrast remained un-indexed and no detectable misindexing occurred. A minor amount of non-indexed points were due to surface topography generated by severe etching during colloidal silica polishing. No second phases were detected. Indexing was sufficient in most grains to reliably infill non-indexed points using a nearest neighbour algorithm (down to six nearest neighbours), which increased the indexed points from 30 % to 70 % without generation of significant artefacts. Most non-indexed points in all of the EBSD maps were due to surface topography associated with fractures and grains plucked during polishing.

Post-processing was done using Channel 5 Tango, and included removal of isolated erroneous points (wildspike correction) and zero solution extrapolation to 6 nearest neighbours. Comparison of the final data with band contrast map (a graphical representation of EBSD quality) by visual inspection shows that no significant artefacts were generated. Grains were detected after noise reduction using a 10° threshold.

Pole figures are shown in the kinematic X-Y-Z reference frame (see Fig. 2i), where X-Y represents the foliation plane. Pole figures were contoured based on total data rather than one point per grain to give a better representation of the volumetric characteristics that are key for velocity anisotropy calculations. A slight distortion of the PMDH04 map due to charging-related drift was corrected using an optical photomicrograph as reference. Note that such drift issues do not affect the crystallographic orientation data collected by EBSD.

4.2. Seismic property determination

Bulk properties of a polycrystalline rock are commonly calculated by Voigt and Reuss elastic bounds (Mainprice, 1990; Mainprice and Humbert, 1994; Lloyd and Kendall, 2005). This method is based on the single-crystal elastic stiffness coefficients and density, the modal proportions and the CPO for each mineral constituent. The elastic properties are averaged over the CPO of each mineral, according to their volumetric fraction, using the geometric-mean averaging method (Mainprice, 1990). This way, the combined stiffness matrix and density of the polycrystalline aggregate are obtained and seismic properties can be derived by solving the Christoffel equation, which is a solution of the wave propagation equation. This yields the three-dimensional distribution of the compressional-wave propagation velocity (V_P) and both the fast (V_{S1}) and slow (V_{S2}) shear-wave propagation velocities. Shear-wave splitting (ΔV_S) is given by,

$$\Delta V_S = |V_{S1} - V_{S2}|, \tag{1}$$

which can be used as a diagnostic of seismic anisotropy (Crampin, 1985). Seismic velocity anisotropy for P wave (AV_P) and for S wave (AV_S) are commonly calculated as,

$$AV_P = 200\,\frac{(V_{P,max} - V_{P,min})}{(V_{P,max} + V_{P,min})}, \tag{2}$$

and

$$AV_S = 200\,\frac{(V_{S1,max} - V_{S2,min})}{(V_{S1,max} + V_{S2,min})}. \tag{3}$$

This methodology has been extensively applied to determine seismic properties of various polycrystalline rocks (Lloyd and Kendall, 2005; Valcke et al., 2006; Lloyd and Kendall, 2005; Tatham et al., 2008; Lloyd et al., 2009; Dempsey et al., 2011). We derived the seismic properties of our samples from the measured CPO with EBSD and the mineral modal proportions determined by optical microscopy by following this methodology. This way, we assessed the effect of microstructure on the bulk seismic properties of our selected samples. To quantitatively assess the bulk seismic properties of a polymineralic evaporite due to its mineralogical composition alone we then adopted a rock-recipe approach based on the method described above. This was carried out by systematically varying the modal proportions of the mineral phases, whilst keeping all crystal orientations perfectly aligned to the reference frame (e.g., Tatham et al., 2008; Healy et al., 2009).

4.3. Ultrasonic velocity measurements

Ultrasonic velocity measurements were made on the same samples analysed by EBSD (plus several additional samples) along the three principal orthogonal X-Y-Z directions to assess the grain-scale effects contributing to the total anisotropy (Table 1; Fig. 2i). Test instrumentation included a pulse generator-receiver unit, two pairs of piezoelectric transducers (one emitter and one receiver of 2.54 cm diameter, and up to 1 MHz oscillation frequency) and a digital oscilloscope (Fig. 3). The compressional-wave transducer (Panametrics V103) was vertically polarised and its maximum sensitivity is normal to the contact face. The

shear-wave transducer (Panametrics V153) was horizontally polarised so that its maximum sensitivity was parallel to the contact face. Bench-top velocity measurements were taken on dry samples, under ambient laboratory conditions of temperature and pressure.

[Figure 3 about here.]

Velocities were determined by using the ultrasonic pulse transmission method (Birch, 1960), consisting of picking the first-arrival travel time of an acoustic signal, which has propagated through a medium. The procedure to measure the propagation speed of ultrasonic waves involved placing a rock sample between the two transducers, then the pulse generator sends an electrical signal to the emitter, which oscillated at 1 kHz frequency. The vibration propagates through the sample and is received by the transducer at the other end. Thus the propagation velocity v for each type of wave is calculated by linear regression of the relation $v = l/t$, by measuring the transit time of the transmitted signal t and the distance it travelled through, i.e., the length l of the sample.

Calibration of the ultrasonic velocity measurements was done using a cuboid piece of pure, solid aluminium, whose V_P is known at 6.35 km/s and V_S at 3.12 km/s (Song et al., 2004). The standard deviation after five repeated measurements using the aluminium block was of 0.1 %. Measurement of ultrasonic wave velocities is a common procedure for rock characterisation (Mah and Schmitt, 2003; Lo et al., 1986), since measurements are highly accurate and easily obtained. For homogeneous and dry materials, velocity is independent of the wave frequency and the shape of the signal does not change greatly during its propagation (Popp and Kern, 1998). However, for heterogeneous rocks, there are important implications because the transmitted wave can be significantly distorted due to the energy scattering produced by the heterogeneities in the rock. In our measurements, the largest source of error was the accuracy and reproducibility in the identification of the first-arrival travel times, this being more difficult for S-wave than for P-wave arrival times (Fig. 3). This is mainly due to the polarisation of S waves into fast and slow velocity components in heterogeneous media; but also due to the interference of the S wave with a faster, interface-induced P-wave signal.

Equations 2 & 3 are expressions commonly used to quantify velocity variation (also known as coefficient of anisotropy), which is defined as the fractional difference between the maximum and minimum velocities in different directions, usually expressed in percentage (Sheriff, 2002). These expressions were used to approximate seismic anisotropy from velocity measurements taken at three orthogonal directions only (Table 1) and to compare with those calculations based on microstructure. Note that to fully determine the azimuthal seismic anisotropy, velocity measurements are required in at least five directions (see Lloyd and Kendall, 2005).

5. Results

5.1. Microstructure and modal content

Sample PMDH01 consists mainly of halite (∼ 95 %). Large (2-6 mm) elongated grains dominate the microstructure. Smaller (<1 mm) halite grains occur along grain boundaries and triple junctions (Fig. 4a-b). Typically, up to 10° crystallographic misorientation is accommodated within grains, and grains are bound by curved to straight high-angle (>10°) boundaries (Fig. 4d). The grains are strongly aligned parallel to a foliation, and typically have aspect ratios of 2:1 to 3.5:1 when viewed normal to the foliation plane (Fig. 4d). A small amount of anhydrite grains (<5 %), of <500 μm size, decorate some of the boundaries of the larger halite grains Fig. 4a. These were not indexed by EBSD. A weak CPO is preserved by halite, in which two of the {100} commonly align with the foliation plane (Fig. 4e). Sets of transgranular fractures cut across the halite grains at high angles to the foliation (Fig. 4d).

[Figure 4 about here.]

The microstructure of PMDH04 consists of interlocking 1-3 mm long grains of halite (∼95 % modal proportion) that are strongly aligned, defining a foliation (Fig. 5a-b). The grains generally contain a small degree (<5°) of internal crystallographic misorientation, and grain boundaries range in morphology from curved to segmented to straight. When measured perpendicular to the foliation plane X-Y, the grains typically are elliptical with aspect ratios of 1.5:1 to 3.5:1 (Fig. 5d). This halite specimen does not preserve a significant CPO (Fig. 5e). This lack of CPO, despite the shape preferred orientation (SPO), has been associated with deformation of salt by dissolution-precipitation creep, in which case there is no, or weak, CPO development (Wenk et al., 2004; Desbois et al., 2010). A small amount of solid inclusions (<5 %) were observed along grain boundaries, showing irregular, occasionally wavy, highly birefringent structures. The size of these solid inclusions ranged from a few dozen micrometers to few millimetres (Fig. 5a). SEM analysis indicated the presence of K, Mg, Cl, Ca, Fe, and S in trace amounts, which suggest the presence of minerals such as sylvite, carnallite, anhydrite and hematite. These were not indexed with EBSD.

[Figure 5 about here.]

PMDH02 and PMDH03 samples consist mainly of anhydrite (∼98 %) and lesser amount of gypsum (∼2 %). The microstructure of PMDH02 shows a predominant grain size of 30-150 μm (Fig. 6a-d). The grains vary in size over short distances and generally have straight boundaries, good triple junctions, and virtually no internal orientation variations (Fig. 6b-d). Grain aspect ratios range from 1:1 to 3.5:1 without a clear SPO (Fig. 6e-h). Anhydrite preserves a moderate to strong CPO such that poles to {100} are strongly aligned in the X-Y plane (i.e., foliation plane) and poles to {001} form a strong cluster that is highly oblique to the X-Y plane, with a maxima at ∼20° from the Z direction (Fig. 6i).

[Figure 6 about here.]

Sample PMDH03 has very narrow grain size range of 40-110 μm. The grains have straight boundaries, good triple junctions, and no internal orientation variations (Fig. 7a-d). The grain shapes normal to the foliation plane have very low aspect ratios (mostly less than 1.5:1) that are predominantly aligned at $\sim 45^\circ$ to the foliation visible in the thin section (Fig. 7e-h). Anhydrite shows a strong CPO, such that poles to {100} are aligned parallel to Y in Fig. reffig:ebsd03i. Poles to {001} form a strong cluster oblique to Y, with a maximum density at $\sim 30^\circ$ from the X direction.

[Figure 7 about here.]

The microstructure of BCDH02 consists mainly of gypsum ($\sim$95 %) with grain sizes typically ranging 50-250 μm (Fig. 8a-b). The grains have aspect ratios of 2:1 to 3:1 (Fig. 8c) and have a bimodal shape preferred orientation with grains aligned along the foliation and at 45° to the foliation (Fig. 8d). Gypsum shows a strong CPO such that poles to {100} cluster parallel to X and poles to {010} cluster parallel to Z (i.e., perpendicular to the foliation), (Fig. 8e). No secondary phases were identified.

[Figure 8 about here.]

5.2. Seismic properties of single crystals

Bulk seismic velocity anisotropy in polymineralic rocks depends directly on the elastic properties, volume fraction, and CPO of each mineral constituent. To understand the velocity distribution and resulting anisotropy in polymineralic evaporites, seismic properties of each mineral phase must first be understood. The seismic velocities of single crystals of halite, anhydrite and gypsum minerals were calculated using the elastic stiffness coefficients and densities from Bass (1995). The mineral form and stereographic projections for compressional velocity (V_P), shear-wave splitting (ΔV_S) and fast shear wave (V_{S1}) polarisation are shown in Fig. 9. Maximum anisotropy values are indicated in percentage below each plot. The crystal symmetry of each mineral controls the symmetry of the velocity distribution. P-wave seismic velocities are highest for anhydrite, then gypsum and halite, successively. For a halite single crystal, the directions of fastest propagation of the compressional wave are parallel to the symmetry axes $a\,b\,c$ and slowest oblique to these axes (Fig. 9a). For anhydrite, the fastest direction of P-wave propagation is parallel to b and the slowest subparallel to c (Fig. 9b). For gypsum, propagation is faster subparallel to a and slowest subparallel to c (Fig. 9c). In terms of the shear-wave splitting, it is maximum oblique to the symmetry axes $a\,b\,c$ for halite; anhydrite exhibits maxima parallel to a and b and minimum around c; gypsum shows a maximum parallel to a and minimum near c. These single-crystal anisotropy values suggest that a small proportion of crystallographically-aligned anhydrite or gypsum will increase the bulk seismic anisotropy of a polycrystalline evaporite. Also, both minerals will tend to make the foliation plane the fastest direction of propagation of compressional wave and increase the shear-wave splitting of the polycrystal.

[Figure 9 about here.]

5.3. Determination of seismic velocities by a 'rock recipe' approach

In order to quantify the influence of each mineral on the whole rock velocity properties, we have applied a rock recipe approach, similar to that of Tatham (2008); Tatham et al. (2008); Lloyd et al. (2009). The calculation follows that used to determine the single crystal velocity distributions, except that the volume fractions of halite, anhydrite and gypsum are varied accordingly. The models in this study are developed for aggregates consisting of 500 grains with CPO such that all mineral phases are perfectly aligned with one another, i.e., a and b axes of different grains are always parallel to one another (Fig. 10c), and that these directions remain constant regardless of the relative mineral proportions. Implicitly, all crystals of all mineral phases would have developed exactly the same CPO during deformation (e.g., salt flow). Although, in natural polymineralic rocks, each mineral phase can develop an independent CPO due to its crystallographic symmetry, this assumption on the CPO allows us to quantify the contribution to the total seismic properties by the composition factor alone. Ternary plots were produced to show the variation of the anisotropy degree for any mixture of the three mineral constituents (Fig. 10a). The bulk anisotropy values increase proportionally to the content of gypsum and anhydrite. However, compressional velocity anisotropy for gypsum-dominated polymineralic aggregates decreases with increasing content of anhydrite up to a volumetric fraction of 30 % anhydrite; for larger modal content of anhydrite, anisotropy increases again (Fig. 10b). A similar destructive behaviour is observed for shear velocity anisotropy, but the threshold volumetric fraction is now at 10 % anhydrite content. Similar effects on the bulk seismic anisotropy between two (non-evaporitic) mineral phases have been reported for EBSD-derived CPOs from natural samples elsewhere (Ward et al., 2012).

For instance, an aggregate made of 90 % Halite and 10 % anhydrite yields anisotropies of 11.8 % for AV_P and of 23.6 % for AV_S (Fig. 10c). These anisotropy magnitudes are 1.5 times larger than those calculated for halite single crystal alone (Fig. 9a). Implicit in the computed velocity predictions is that the contribution of cracks and pores are not considered. Thus, the modelled results only give a value for the velocity anisotropy arising from the intrinsic mineralogical rock properties of perfectly aligned grains. Therefore, quantification of fabrics using EBSD measurements is required to improve our understanding of the effect of CPO on the bulk seismic anisotropy of natural polymineralic evaporites.

[Figure 10 about here.]

5.4. Determination of seismic properties from EBSD data

Using the CPO data acquired by EBSD analysis of the selected samples (Figs 4,5,6,7, & 8), the single-crystal elastic properties of halite, anhydrite and gypsum (Bass, 1995), and their modal proportions, the seismic properties were calculated. These samples were quasi-monomineralic, which is a situation that allows resolution of the influences of the CPO (as computed form the EBSD-measured CPO) from other properties,

such as SPO, pores, grain boundary structure, etc. The calculations give an intrinsic value arising from crystal alignment only, complementing the results previously obtained where composition was the variable. Results of the distribution of the calculated V_P, ΔV_S and V_{S1} direction of polarisation, caused by the CPO of these samples are shown in Fig. 11. Stereographic projections of velocities are oriented according to the sample reference frame. For clarity, the trace of the foliation is indicated by a thick black line in the diagram at the top of the figure.

[Figure 11 about here.]

The orientation distribution of velocities for halite sample PMDH01 (Fig. 11a) clearly reflects halite single-crystal property distribution (Fig. 9a), slightly rotated. The measured CPO of halite is weak (Fig. 4e), resulting in low anisotropy values (AV_P 2.64 %, AV_S 6.76 %). Similarly, seismic property distribution for sample PMDH04 (Fig. 11b) is derived from a measured near random crystal orientation (Fig. 5e), which disperse the single-crystal velocity distribution, further reducing the anisotropy. Despite the well-defined SPO (Fig. 5c-d), bulk anisotropy values are very low (AV_P at 0.69 % and AV_S at 1.64 %). The polarisation of the fast shear wave (V_{S1}) for both halite samples are disturbed from that of single crystal.

Seismic velocities of anhydrite sample PMDH02 (Fig. 11c) show girdle-like maxima V_P and maxima ΔV_S on the girdle, which are subparallel to the foliation, as a result of its moderate CPO (Fig. 6i). Minima V_P cluster parallel to the foliation plane whereas minima ΔV_S are disperse. Despite the highly anisotropic velocities of anhydrite single crystal (AV_P 42.98 %, AV_S 83.25 %, Fig. 9b), anisotropies derived from its microstructure are low (AV_P 5.58 %, AV_S 6.47 %). The velocity distribution predicted for anhydrite sample PMDH03 shows both maxima V_P and maxima ΔV_S clustered normal to the foliation plane. Minima V_P cluster around Y-axis, parallel to the orientation of foliation (Fig. 11d), reflecting the strong measured CPO (Fig. 7i). Anisotropy values are 8.92 % for AV_P and 7.78 % for AV_S.

Finally, the velocity distribution for the gypsum mylonite BCDH02 (Fig. 11e), resulting from a strong CPO (Fig. 8e), shows maxima V_P clearly parallel to foliation and minima V_P normal to the foliation. Distribution of ΔV_S shows a wide area of maxima perpendicular to the foliation plane, whereas minima ΔV_S cluster parallel to the foliation. Values of anisotropy are 13.48 % for AV_P and 22.29 % for AV_S, which are about a third of those anisotropy values calculated for gypsum single crystal (Fig. 9c).

5.5. Laboratory measurements of ultrasonic velocity

Seismic velocity measurements of the full data set for the X-Y-Z directions are listed in Table 1. Plots in Fig. 12 show comparisons of V_P, V_S, AV_P and AV_S between the CPO-calculated and the ultrasonic-measured properties. The background colour shade indicates the dominant mineralogy of the samples, indicated in the legend at the bottom of the figure. Velocity data points represented with filled symbols are the average wave speed parallel to the foliation plane taken from measurements along X and Y directions, and those

with open symbols are velocity measurements taken perpendicular to the foliation plane X-Y, i.e., along the Z direction (Figs. 12a,b). Error bars are the standard deviation. As for the anisotropy plot (Fig. 12c), filled symbols are AV_P and open symbols are AV_S.

[Figure 12 about here.]

The halite single crystal (PMDH06) has average velocities of V_P=4.6 km/s and V_S=2.4 km/s, which are in agreement with velocity values found in the literature for halite at ambient pressure (Sun et al., 1991). V_P measured in both coarse-grained halite samples show consistently larger values when measured parallel to Z direction, (Fig. 12), caused by long grains aligned preferentially on the X-Y plane (Fig. 2g). V_S measurements, on the contrary, produced lower values perpendicular to this fabric. Measured AV_P were of 5.82 % and 7.28 % and AV_S were of 9.09 % and 8.36 %, for PMDH01 and PMDH04, respectively (Table 1), where anisotropies were computed from Eqs. 2 & 3. For both halite samples, the CPO-calculated velocity magnitudes were higher than those measured in the laboratory, since ultrasonic velocity are attenuated by the grain boundaries and porosity. Conversely, the CPO-calculated anisotropy magnitudes were lower than the total anisotropy obtained from ultrasonic measurements (see Table 1). The difference between these two anisotropy values can give an estimate of the fraction of the total anisotropy caused by structural elements such as SPO and cracks altogether, being of 3.18-6.59% for AV_P and 2.33-6.7% for AV_S.

Maximum velocities of wave propagation measured on both anhydrite samples (PMDH02 and PMDH03) are the highest values among the test materials (V_P from 5.8 to 6.1 km/s and V_S from 2.6 to 3.3 km/s, Fig. 12). Such values are in agreement with laboratory measurements reported in the literature (e.g., Trippetta et al., 2010). Anisotropy of P-wave for both anhydrite samples are <2.5 %, but their S-wave velocity anisotropies vary from 1.5 to 16 %. This difference in AV_S may be due to the presence of a crack across PMDH03 sample, parallel to the lamination (see scanned thin section in the upper right of Fig. 7), that perturbs the shear wave propagation (Crampin, 1985). However, the fast and slow shear-wave velocities could not be distinguished during first-arrival time picking, so wave splitting was not calculated. In agreement with previous studies (Trippetta et al., 2010), depositional bands observed in anhydrite (Fig. 2h) do not to exert significant velocity variation at laboratory pressure conditions. CPO-calculated V_P of both anhydrite samples are in agreement with those from ultrasonic tests (Table 1), while CPO-calculated V_S are higher.

Velocities for the gypsum mylonite samples showed a marked variation with the direction of measurement, so that the velocities are consistently faster in directions parallel to foliation than those perpendicular to the foliation plane (Fig. 12, Table 1). This behaviour has been documented with experimental determination of ultrasonic velocities in foliated carbonate evaporites (e.g., Burlini and Kunze, 2000). Anisotropy estimates for gypsum mylonites are highest for those showing nodular and lozenge dominant fabrics (e.g. BC and FP outcrop samples, Fig. 2a-e), ranging from 4.68 to 17.6 % for AV_P, and from 4.5 to 18.4 % for AV_S. Samples with larger content of anhydrite (e.g., samples CMP01b-c and BCDH04, Table 1) have the lowest

anisotropies (1.37-3.48 % for AV_P, and 0.82-13.8 % for AV_S). These results are strongly controlled by the presence and orientation of porosity and open cracks, since ultrasonic measurements were taken at room pressure and temperature. Therefore, low anisotropy values are directly associated with less porosity and therefore higher bulk density caused by anhydrite content, a relationship that is in agreement with that observed from the rock recipe ternary plots (Fig. 10b). This relationship is also supported by the density and velocity measurements in Table 1. CPO-calculated velocities are higher that those from ultrasonic test. Differences between CPO-calculated and ultrasonic-measured anisotropy are 2.7 % for AV_P and 30.8 % for AV_S. Note that the largest standard deviation registered was for V_S of the BCDH01 sample (equivalent to BCDH02 sample). This is because of the difficulty in the first-arrival travel time picking. Contamination of the acoustic signal may have been caused by edge reflexions and diffractions (Qixian and Bungey, 1996) since this was the smallest cuboid among the sample suite.

Summary of the density calculations, ultrasonic velocity measurements and their corresponding anisotropies (indicated in data type as *Ultra* for brevity) are listed in Table 1. Velocity measurements are according to the sample reference frame (Fig. 2i). For comparison, the CPO-derived velocities and anisotropies (indicated in data type as *CPO*) are also included. Such data correspond to V_P and V_{S1} values; on the velocity stereographic projections X and Y components represent the foliation plane and Z the normal to this plane (Fig. 11). Single crystal calculated seismic properties are indicated in data type as *Single*. Density calculations are generally lower than that of the single crystals, probably due to inaccuracies in the volume determination of the cube-shape samples.

[Table 1 about here.]

6. Discussion

The degree of seismic anisotropy in evaporite samples from Nova Scotia was found to be controlled by their CPO. Increasing modal proportion of highly elastically anisotropic minerals can enhance or attenuate seismic anisotropy, depending on their relative CPO. Other factors, such as porosity, SPO and oriented cracks contributed between 2.7-6.6 % to the bulk P-wave velocity anisotropy and 2.3-30.8 % to the bulk S-wave velocity anisotropy observed at centimetre scale at ambient laboratory pressure. However, their effects are assumed to diminish with increasing confining pressure.

6.1. Effects of mineralogy on bulk seismic properties

The variation of both AV_P and AV_S, obtained by the rock recipe, suggests that the bulk anisotropies for a halite-dominated evaporite will increase significantly due to a small proportion of anhydrite (Fig. 10b). These results are based on single crystal orientations, i.e., all mineral phases are perfectly aligned to the sample reference frame. In contrast, calculated anisotropy values using the EBSD-derived CPO of PMDH01 sample, whose anhydrite content was <5 %, are lower than those predicted with the rock recipe (Fig. 11a). This is

partly due to the grain boundary effects that attenuate the seismic properties of a polycrystalline aggregate, compared to those properties of the single crystal (Lloyd and Kendall, 2005), but also due the weak CPO of halite grains. These calculations were done for 95 % halite proportion and the measured CPO and 5 % anhydrite proportion of randomly oriented grains. Anhydrite crystals growing along halite grain boundaries (Fig. 4a), appear to be randomly oriented, so their effect on the bulk properties will be negligible. This is certainly not surprising since CPO of both mineral phases are near random. Studies conducted elsewhere (Dempsey et al., 2011; Ward et al., 2012) suggest that a small amount of highly anisotropic minerals, strongly oriented, can alter significantly the bulk anisotropy of less anisotropic mineral phase also strongly oriented. Simulations of halite and anhydrite fabrics to determine seismic property variations are to be conducted in further work.

As for mixtures of anhydrite and gypsum, seismic anisotropies predicted with the rock recipe are significantly strong and decrease with increasing content of gypsum (Fig. 10b). Note that the variation of anisotropy strength is non-linear with the proportion of gypsum and, in fact, can cause a destructive interference. AV_P relationship has a minimum at 30 % anhydrite content, reaching an anisotropy value even lower of that of the gypsum single crystal (Fig. 9c). When gypsum content increases, so does the anisotropy strength. This behaviour is less apparent for AV_S variation curve, where the maximum interference occurs at 10 % anhydrite content (Fig. 10b). These observations are in good agreement to recent findings on mutually destructive interference between two (non-evaporitic) mineral phases (Ward et al., 2012). Because these results are based on single crystal orientations, such a destructive interference may change for calculations in gypsum mylonites based on EBSD-derived CPO data; anisotropy magnitudes can be overestimated if single crystal orientations alone are accounted for. To this stage, predictions provided insights into the mutually destructive interference between gypsum and anhydrite but calculation constrained by microstructural data must be studied further. Moreover, ultrasonic measurements suggest that velocity anisotropy decreases with anhydrite content for gypsum-dominated samples (Table 1), behaviour that agrees with that observed from the rock recipe approach.

6.2. Effects of CPO on bulk seismic properties

Calculations from EBSD-derived CPO data yielded low velocity anisotropy values for both PMDH01 and PMDH04 halite-dominated samples (Table 1), resulting from their weak and near random CPOs (Figs. 4e & 5e), and demonstrating the strong dependency of seismic properties on microstructure. Random crystal orientation in polycrystalline halite with well-defined SPO has been previously documented (Urai et al., 2008). This is believed to be caused by dissolution-precipitation creep and not by dislocation creep (Wenk et al., 2004; Desbois et al., 2010). This also supports the previous assumption on anhydrite crystals (along grain boundaries) that lack CPO. Nevertheless, natural halite can develop strong CPO, depending on the local tectonic stress regime acting in the subsurface (Raymer and Kendall, 1997; Raymer et al.,

2000b,a). For instance, simulating typical fabrics developed under simple shear and axial extension can yield low AV_P values (3.75-4.75 %, respectively) for polycrystalline (100 %) halite with a strong CPO (Raymer et al., 2000b). Initially, these anisotropy predictions may suggest that the intrinsic seismic anisotropy of halite will have little effect on the bulk seismic anisotropy of polymineralic evaporites. Although halite is the main constituent of salt in the subsurface, as is generally assumed, there will be secondary mineral phases, which may or may not have developed a CPO. To our knowledge, the influence of strongly oriented, highly anisotropic evaporitic minerals in naturally deformed (halite-dominated) evaporites has not been yet documented.

CPO-derived seismic anisotropies for both quasi-monomineralic anhydrite samples PMDH02 and PMDH03 are controlled by their CPOs (Figs. 6i & 7i); they are much lower than those for the single-crystal end-members. Ultrasonic V_P of these samples agree with those calculated from their CPO, which suggests that the contribution of lamination in anhydrite (Fig. 2h) does not affect the AV_P at ambient pressure. Such observations are in good agreement with ultrasonic measurements in foliated anhydrite that yielded low anisotropy values (Trippetta et al., 2010). The presence of large and oriented cracks in the sample PMDH03 attenuates significantly V_S (Fig. 12b). Total measured anisotropies are higher than those derived from CPO data.

Seismic anisotropies for the gypsum mylonite BCDH02 were the highest calculated from EBSD-derived CPO data as a result of its strong CPO (Fig. 8). Fabrics observed in the field indicate that gypsum can become crystallographically oriented easily during deformation, producing strong mylonitic fabrics. Those gypsum mylonites with anhydrite content (CMP samples) have higher ultrasonic velocities than those richer in gypsum (BC, FP, PH samples), (see Table 1). More studies on the effects of secondary mineral phases will be conducted to gain insight into the seismic variation interference in polymineralic evaporites consisting of various mixtures of anhydrite and gypsum content.

6.3. Effects of extrinsic factors on bulk seismic properties

We emphasise that the method to derive seismic properties from CPO does not account for structural features such as (grain) shape preferred orientation (SPO), pore shape and alignment, oriented cracks or fractures or even layering (Wenk et al., 2004), all of which can be sources for seismic anisotropy and affect directly the ultrasonic measurements at ambient conditions. To quantify their individual contribution to the total anisotropy of a polycrystalline rock is difficult because different mechanisms can produce anisotropy at multiple scales. This study benefits from measurements at microscale and mesoscale taken from the same rock specimens. Thus, the difference between the CPO-derived and ultrasonic seismic anisotropies can give us an estimate of the total fraction of the bulk anisotropy due to CPO. Such differences are between 2.7-6.59 % for AV_P and 2.33-30 % for AV_S, which are significant relative to the anisotropy degrees that we have observed all through this study. Since our ultrasonic tests were conducted at room pressure conditions, discrepancies

between calculated and measured velocities may be reduced at higher confining pressures (Fig. 12a-b). The behaviour observed in ultrasonic seismic velocity of gypsum mylonites, where the direction of fast seismic wave propagation is parallel to the foliation, is in agreement with calculated velocities for the gypsum single crystal (Fig. 9c) and also from the CPO-derived seismic properties (Fig. 11e). However, to fully support this, microstructural analyses must be carried out on more gypsum mylonite samples and determine if this behaviour is derived from crystallographic orientations.

The relationship between CPO and SPO, and the effects on seismic velocity anisotropy, are poorly understood, not only in evaporites but in sedimentary rocks in general (e.g. Valcke et al., 2006). While CPO is arguably the controlling factor of intrinsic anisotropy, SPO is an important contributor to the total anisotropy measured with ultrasonic velocity tests (e.g. Burlini and Kunze, 2000). Such shape fabric and grain orientations in evaporites are observed in hand specimens and at the outcrop scale (Fig. 2). Differences between CPO-calculated and ultrasonic-measured anisotropies provide a proxy for the relative (combined) contribution of SPO, cracks and pores present in our samples. Further investigation of SPO in evaporites will be considered for a more comprehensive analysis on the extrinsic sources of anisotropy in evaporites.

Finally, evaporite sequences often occur in nature as interlayered deposits of, for example, halite, anhydrite, gypsum, sylvite, carnallite, among others. Fabrics can developed at depth as a result of evaporite ductile deformation: the nearer to the sheared contact zones, the stronger the development of boudinage structures and mylonitic fabrics are expected. Thus, we suggest to incorporate the seismic properties derived from microstructural data of the individual mineral constituents to constrain quantitative anisotropic models of evaporites, this will provide more realistic descriptions of their effects in a larger scale. A better understanding of the relationship between the sources of anisotropy at various scales and the acquisition of seismic parameters, such as Thomsen's anisotropy parameters (Thomsen, 1986), can allow evaporite seismic anisotropy incorporation into geological and geophysical applications.

7. Concluding statements

In this study, a suite of natural evaporite samples rich in halite, anhydrite and gypsum, from a single diapiric province, was used to explore the seismic velocity variations due to microstructural and compositional properties. It benefits from observations at both micro and mesoscale on the same evaporite samples, at which seismic velocity anisotropy may differ. Three lithologies were investigated to emphasise the mineralogical heterogeneity that characterises most evaporitic deposits, in contrast to previous studies that have focused on natural halite only. By comparing the total seismic anisotropy observed from ultrasonic velocity measurements at laboratory pressure conditions with the velocity anisotropy calculated from crystallographic preferred orientations, we provide a proxy for the relative contribution of structural characteristics such as shape preferred orientation, cracks and pores to the seismic velocity anisotropy of evaporites. Our observations complement previous studies which have studied the intrinsic (i.e. CPO) or the extrinsic (e.g. SPO,

cracks, pores, layering) sources of velocity anisotropy in evaporites either individually or collectively. Insights into the complex relationship between CPO and SPO in evaporites have been obtained.

The analyses conducted in this study lead to the following conclusions:

1. Crystallographic preferred orientation is responsible for a significant fraction of the bulk seismic velocity anisotropy of the polycrystalline evaporites under study. This is evident when comparing velocity anisotropy values from EBSD-derived CPO to calculations from the rock recipe based on single crystals. Velocity anisotropy calculated from the CPO decrease progressively from gypsum mylonite to anhydrite-dominated to halite-dominated samples reflecting the intensity of their CPO.
2. The influence of individual evaporitic minerals on velocity anisotropy depends not only on its modal proportion, but on its individual CPO. A small amount of highly elastically anisotropic, randomly-oriented anhydrite crystals does not exert a significant effect on the bulk anisotropy of a halite-dominated evaporite. Calculations from the rock recipe, however, predict a stronger velocity anisotropy for a small amount of crystallographically-oriented anhydrite crystals.
3. Variation of seismic velocity anisotropy predicted with the rock recipe suggests a mutually destructive relationship between anhydrite and gypsum that, if true, changes the perception that highly anisotropic minerals only enhance anisotropy, when it may also reduce it. The threshold proportion of anhydrite after which seismic anisotropy increases again may change for aggregates of strongly-oriented minerals.
4. Seismic velocity anisotropy caused by extrinsic sources can be as significant as intrinsic velocity anisotropy, and must be taken into account to characterise seismic velocity anisotropy of evaporites.

8. Acknowledgements

We thank Stewart Mac Swain from the Canadian Salt Co. Ltd., Pugwash Mine, for access to the underground workings and facilitate the collection of samples. This study was funded by the National Council for Science and Technology of Mexico (CONACYT) and the Mexican Petroleum Institute (IMP).

9. References

Almqvist, B. S. G., Hirt, A. M., Herwegh, M., Ebert, A., Walter, J. M., Leiss, B., Burlini, L., 2013. Seismic anisotropy in the Morcles nappe shear zone: Implications for seismic imaging of crustal scale shear zones. Tectonophysics 603, 162–178.

Alsop, I., Brown, J. P., Davison, I., Gibling, M. R., 2000. The geometry of drag zones adjacent to salt diapirs. Journal of the Geological Society 157, 1019–1029.

Aptukov, V. N., Konstantinova, S. A., Skachkov, A. P., 2010. Micromechanical characteristics of karnallite, sylvinite and rock salt at Upper Kama deposit. Journal of Mining Science 46 (4), 352–358.

Bass, J. D., 1995. Elasticity of minerals, glasses, and melts. AGU Reference Shelf 2, 45–63.

Birch, F., 1960. The velocity of compressional waves in rocks to 10 kilobars, part 1. Journal of Geophysical Research 65 (4), 1083–1102.

Boeyens, J., Ichhram, V., 2002. Redetermination of the crystal structure of calcium sulphate dehydrate, CaSO4-H2O. Zeitschrift fuer Kristallographie 27, 9–10.

Burlini, L., Kunze, K., 2000. Fabric and seismic properties of Carrara marble mylonite. Physics and Chemistry of the Earth, Part A: Solid Earth and Geodesy 25 (2), 133–139.

Crampin, S., 1985. Evaluation of anisotropy by shear-wave splitting. Geophysics 50 (1), 142–152.

Dempsey, E. D., Prior, D., Mariani, E., Toy, V. G., Tatham, D. J., 2011. Mica-controlled anisotropy within mid-to-upper crustal mylonites: an EBSD study of mica fabrics in the Alpine Fault Zone, New Zealand. Geological Society, London, Special Publications 360, 33–47.

Desbois, G., Závada, P., Schléder, Z., Urai, J. L., 2010. Deformation and recrystallization mechanisms in actively extruding salt fountain: Microstructural evidence for a switch in deformation mechanisms with increased availability of meteoric water and decreased grain size (qum kuh, central iran). Journal of Structural Geology 32 (4), 580–594.

Hawthorne, F., Ferguson, R., 1975. Anhydrous sulphates ii - refinement of the crystal structure of anhydrite. Canadian Mineralogist 13, 289–292.

Healy, D., Reddy, S. M., Timms, N. E., Gray, E. M., Brovarone, A. V., 2009. Trench-parallel fast axes of seismic anisotropy due to fluid-filled cracks in subducting slabs. Earth and Planetary Science Letters 283 (1-4), 75 – 86, doi: http://dx.doi.org/10.1016/j.epsl.2009.03.037.

Hildyard, R. C., Prior, D. J., Faulkner, D. R., Mariani, E., 2009. Microstructural analysis of anhydrite rocks from the Triassic Evaporites, umbria-marche apennines, central italy: An insight into deformation mechanisms and possible slip systems. Journal of Structural Geology 31 (1), 92–103, doi: http://dx.doi.org/10.1016/j.jsg.2008.10.009.

Howie, R. D., 1986. Windsor group salt in the Cumberland Basin of Nova Scotia. Geological Survey of Canada.

Kupfer, D. H., 1989. Gypsum dehydration, agent of salt diapirism. Gulf Coast Association of Geological Societies Transactions 39, 171–181.

Lloyd, G., Butler, R., Casey, M., Tatham, D., Mainprice, D., 2011a. Constraints on the seismic properties of the middle and lower continental crust. Geological Society, London, Special Publications 360 (1), 7–32.

Lloyd, G., Kendall, J.-M., 2005. Petrofabric-derived seismic properties of a mylonitic quartz simple shear zone - implications for seismic reflection profiling. Geological Society, London, Special Publications 240 (1), 75–94.

Lloyd, G. E., Butler, R. W., Casey, M., Mainprice, D., 2009. Mica, deformation fabrics and the seismic properties of the continental crust. Earth and Planetary Science Letters 288 (1), 320–328.

Lloyd, G. E., Halliday, J., Butler, R. W., Casey, M., Kendall, J.-M., Wookey, J., Mainprice, D., 2011b. From crystal to crustal: petrofabric-derived seismic modelling of regional tectonics. Geological Society, London, Special Publications 360 (1), 49–78.

Lo, T.-w., Coyner, K. B., , Toksoz, M. N., 1986. Experimental determination of elastic anisotropy of Berea sandstone, Chicopee shale, and Chelmsford granite. Geophysics 51, 164–171.

Louis, L., David, C., Metz, V., Robion, P., Menéndez, B., Kissel, C., 2005. Microstructural control on the anisotropy of elastic and transport properties in undeformed sandstones. International journal of rock mechanics and mining sciences 42, 911–923.

Mah, M., Schmitt, D. R., 2003. Determination of the complete elastic stiffnesses from ultrasonic phase velocity measurements. Journal of Geophysical Research: Solid Earth (1978–2012) 108 (B1), ECV–6.

Mainprice, D., 1990. A fortran program to calculate seismic anisotropy from the lattice preferred orientation of minerals. Computers and Geosciences 16, 385–393.

Mainprice, D., Humbert, M., 1994. Methods of calculating petrophysical properties from lattice preferred orientation data. Surveys in Geophysics 15 (5), 575–592.

Mainprice, D., Nicolas, A., 1989. Development of shape and lattice preferred orientations: application to the seismic anisotropy of the lower crust. Journal of Structural Geology 11 (1-2), 175–189, doi: http://dx.doi.org/10.1016/0191-8141(89)90042-4.

Popp, T., Kern, H., 1998. Ultrasonic wave velocities, gas permeability and porosity in natural and granular rock salt. Physics and Chemistry of the Earth 23, 373–378.

Prior, D. J., Boyle, A. P., Brenker, F., Cheadle, M. C., Day, A., Lopez, G., Peruzzo, L., Potts, G. J., Reddy, S., Spiess, R., Timms, N. E., Trimby, P., Wheeler, J., Zetterstrom, L., 1999. The application of electron backscatter diffraction and orientation contrast imaging in the SEM to textural problems in rocks. American Mineralogist 84 (11-12), 1741–1759.

Qixian, L., Bungey, J. H., 1996. Using compression wave ultrasonic transducers to measure the velocity of surface waves and hence determine dynamic modulus of elasticity for concrete. Construction and building materials 10, 237–242.

Raymer, D. G., Kendall, J. M., Pedlar, D., Kendall, R. R., Mueller, M. C., Beaudoin, G. J., 2000a. The significance of salt anisotropy in seismic imaging. In: SEG Annual Meeting Expanded Abstract.

Raymer, D. G., Kendall, J.-M. G., 1997. Potential pitfalls in imaging salt structures due to preferred crystal orient at ion and seismic anisotropy. In: SEG Annual Meeting Expanded Abstract.

Raymer, D. G., Tommasi, A., Kendall, J.-M., 2000b. Predicting the seismic implications of salt anisotropy using numerical simulations of halite deformation. Geophysics 65 (4), 1272–1280.

Sheriff, R., 2002. Encyclopedic Dictionary of Exploration Geophysics. Geophysical references series. Society of Exploration Geophysicists.

Song, I., Suh, M., Woo, Y.-K., Tianyao, H., 2004. Determination of the elastic modulus set of foliated rocks from ultrasonic velocity measurements. Engineering geology 72, 293–308.

Sun, Z., Brown, R. J., Lawton, D. C., Wang, Z., 1991. Seismic anisotropy and salt detection: A physical modeling study. In: SEG Annual Meeting.

Tatham, D., Lloyd, G., Butler, R., Casey, M., 2008. Amphibole and lower crustal seismic properties. Earth and Planetary Science Letters 267 (1), 118–128.

Tatham, D. J., 2008. Towards using seismic anisotropy to interpret ductile deformation in mafic lower crust. Ph.D. thesis, University of Leeds.

Thomsen, L., 1986. Weak elastic anisotropy. Geophysics 51 (10), 1954–1966.

Trippetta, F. C., Colletti, S., Vinciguerra, Meredith, P. G., 2010. Laboratory measurements of the physical properties of Triassic evaporites from Central Italy and correlation with geophysical data. Tectonophysics 492, 121–132.

Urai, J., Schléder, Z., Spiers, C., Kukla, P., 2008. Flow and transport properties of salt rocks. In: Litke, R., Bayer, U., Gajewski, D., Nelskamp, S. (Eds.), Dynamics of complex intracontinental basins: the Central European Basin system. Springer-Verlag,

626 pp. 277–290.
627 Valcke, S., Casey, M., Lloyd, G., Kendall, J.-M., Fisher, Q., 2006. Lattice preferred orientation and seismic anisotropy in
628 sedimentary rocks. Geophysical Journal International 166 (2), 652–666.
629 Ward, D., Mahan, K., Schulte-Pelkum, V., 2012. Roles of quartz and mica in seismic anisotropy of mylonites. Geophysical
630 Journal International 190 (2), 1123–1134.
631 Wenk, H., , Van Houtte, P., 2004. Texture and anisotropy. Reports on Progress in Physics 67 (8), 1367.

Table 1: Summary of measured and calculated velocities and anisotropies for the full suite of evaporite samples. Under *Sample* tag, properties of single crystals are indicated as *Single*. Under *Data type* tag, CPO-derived properties are indicated as *CPO*; ultrasonic measurements are indicated as *Ultra*. Dry density is ρ; directions of measurement are X-Y-Z, where X-Y is the foliation plane and Z is normal to the foliation (see Fig. 3 for reference); anisotropy values were calculated using Eqs. 2 & 3; ultrasonic measurements were taken at room pressure and temperature.

Mineral	Sample name	Data type	ρ g/cm^3	V_P (km/s) X	Y	Z	V_S (km/s) X	Y	Z	AV_P %	AV_S %
Halite-dominated	Single		2.163	4.762	4.762	4.762	2.433	2.433	2.433	7.84	17.4
	PMDH06	Ultra	1.992	4.691	4.618	4.618	2.409	2.396	2.396	1.58	0.52
	PMDH01	CPO	2.163	4.605	4.557	4.542	2.602	2.697	2.688	2.64	6.76
	PMDH01	Ultra	2.065	3.909	3.913	4.141	2.258	2.147	2.062	5.82	9.09
	PMDH04	CPO	2.163	4.562	4.556	4.554	2.632	2.633	2.632	0.69	1.64
	PMDH04	Ultra	2.044	3.935	3.837	4.259	2.011	2.130	1.865	7.28	8.36
	PMDH05	Ultra	2.045	4.349	4.238	4.396	2.466	2.449	2.436	3.66	1.22
Anhydrite-dominated	Single		2.963	5.626	6.135	7.902	3.120	2.991	3.312	43.0	83.2
	PMDH02	CPO	2.963	5.930	5.780	6.052	3.493	3.487	3.540	5.58	6.47
	PMDH02	Ultra	2.893	5.998	6.134	6.014	3.325	3.276	3.307	2.24	1.50
	PMDH03	CPO	2.963	6.026	5.677	6.160	3.601	3.429	3.573	8.92	7.78
	PMDH03	Ultra	2.803	5.896	5.882	5.758	2.671	3.143	2.985	2.37	16.1
Gypsum-dominated	Single		2.317	5.858	5.556	5.202	3.316	2.943	2.226	36.1	62.9
	CMP01a	Ultra	3.126	5.281	5.395	6.129	2.765	1.950	2.610	5.73	32.7
	BCDH04	Ultra	2.321	5.208	5.208	5.136	2.854	2.549	2.491	1.37	13.8
	CMP01b	Ultra	2.622	5.455	5.613	5.242	2.829	3.047	2.829	2.87	7.50
	CMP01c	Ultra	2.320	4.991	4.899	4.820	2.553	2.574	2.570	3.48	0.82
	BC07b	Ultra	2.616	4.745	4.576	4.364	2.824	2.707	2.479	8.36	8.58
	BC07d	Ultra	2.197	5.211	5.072	4.726	2.824	2.707	2.479	9.70	12.9
	BC0DH3	Ultra	2.150	5.044	5.114	4.535	2.740	2.717	2.289	11.8	17.5
	PH09	Ultra	2.139	5.104	4.934	4.482	2.687	2.613	2.486	12.8	7.75
	PH10	Ultra	2.179	4.905	4.933	4.348	2.479	2.221	2.561	12.4	14.0
	FP09	Ultra	2.160	4.873	4.780	4.435	2.711	2.684	2.272	9.33	17.2
	FPN02	Ultra	2.105	4.721	4.769	4.550	2.537	2.525	2.424	4.68	4.50
	FPN03	Ultra	2.749	4.788	4.742	3.995	2.644	2.615	2.186	17.6	18.4
	FPN01	Ultra	2.160	4.618	4.703	4.446	2.542	2.516	2.431	5.60	4.40
	BCDH02	Ultra	2.035	4.689	4.477	4.208	2.687	1.822	1.604	10.8	53.1
	BCDH02	CPO	2.317	5.370	5.731	5.133	2.906	2.877	2.847	13.5	22.3

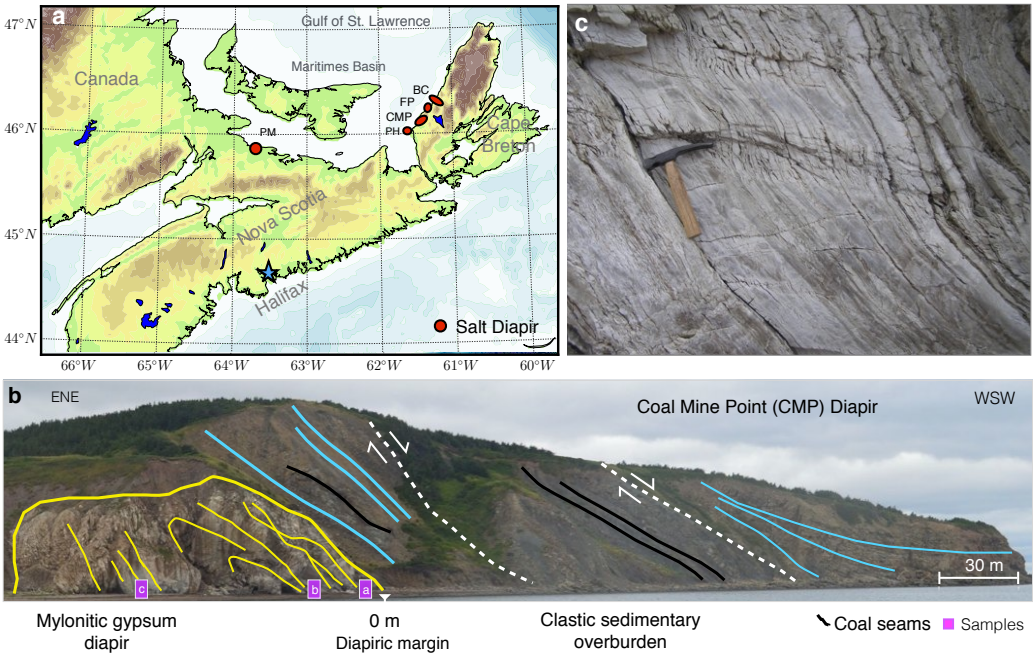

Figure 1: a) Map of the Gulf of St. Lawrence and western Cape Breton showing the localities where we sampled evaporites. b) Simplified cross-section of the salt diapir and its drag zone exposed at Coal Mine Point (CMP), modified from Alsop et al. (2000) Samples were taken from three different places within the diapir (indicated by squares). c) Detail of the intense mylonitic fabric that characterises this gypsum diapir outcrop. Note that foliation is parallel to the diapiric flank. Hammer of 30 cm length for scale.

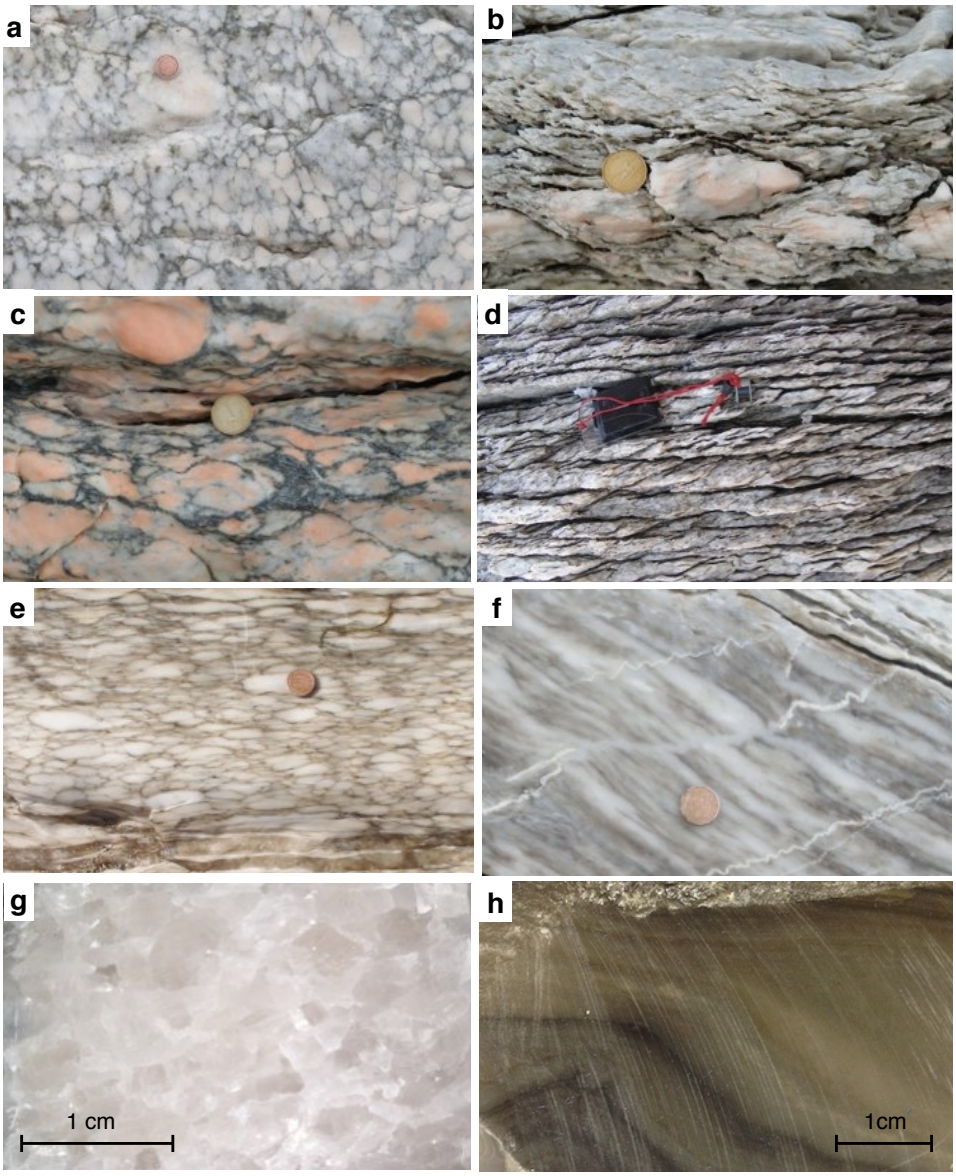

Figure 2: Typical fabrics observed in the salt diapirs under study. a)-c) Moderately to highly deformed nodular gypsum at Finlay Point (FP) and Port Hood (PH) diapir outcrops. d)-e) Mylonitic fabrics of increasing intensity developed in bitumen-stained gypsum at Broad Cove (BC) outcrop. Note the lozenge dominant fabrics. f) Strong mylonitic fabric characterised by white to grey massive gypsum cross-cut by thin and highly deformed veins of gypsum at Coal Mine Point (CMP) outcrop. g) Macrofabric of halite specimen and h) anhydrite sample, both from Pugwash. Coin diameter varies between 2 and 2.5 cm. Clinometer dimensions are 10x6 cm.

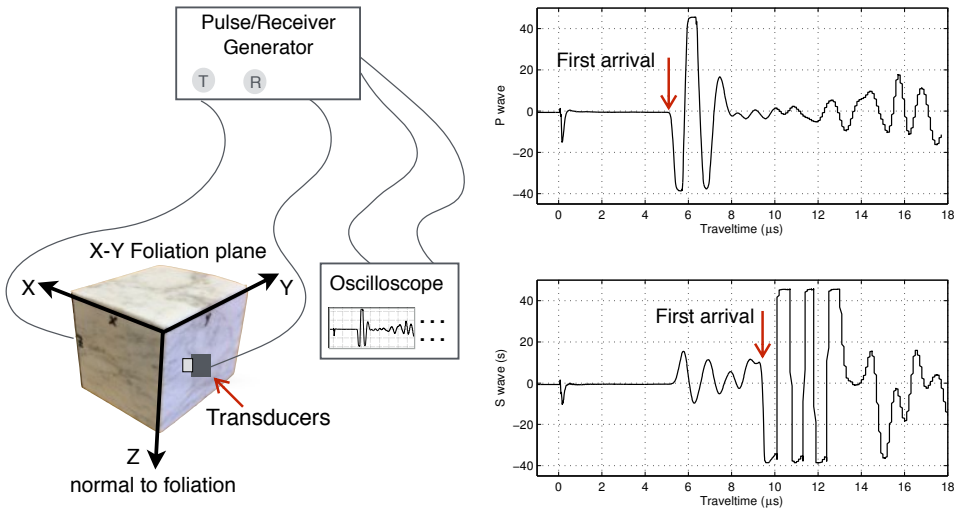

Figure 3: Ultrasonic velocity measurement set-up and sample reference system. Seismic velocities were obtained with the ultrasonic pulse transmission method (Birch, 1960) using up to 1 kHz oscillation frequency. First-arrival travel times were manually picked to calculate the propagation speed of both compressional and shear waves. Velocities were taken for X-Y-Z directions at room conditions of pressure and temperature on cube shaped samples.

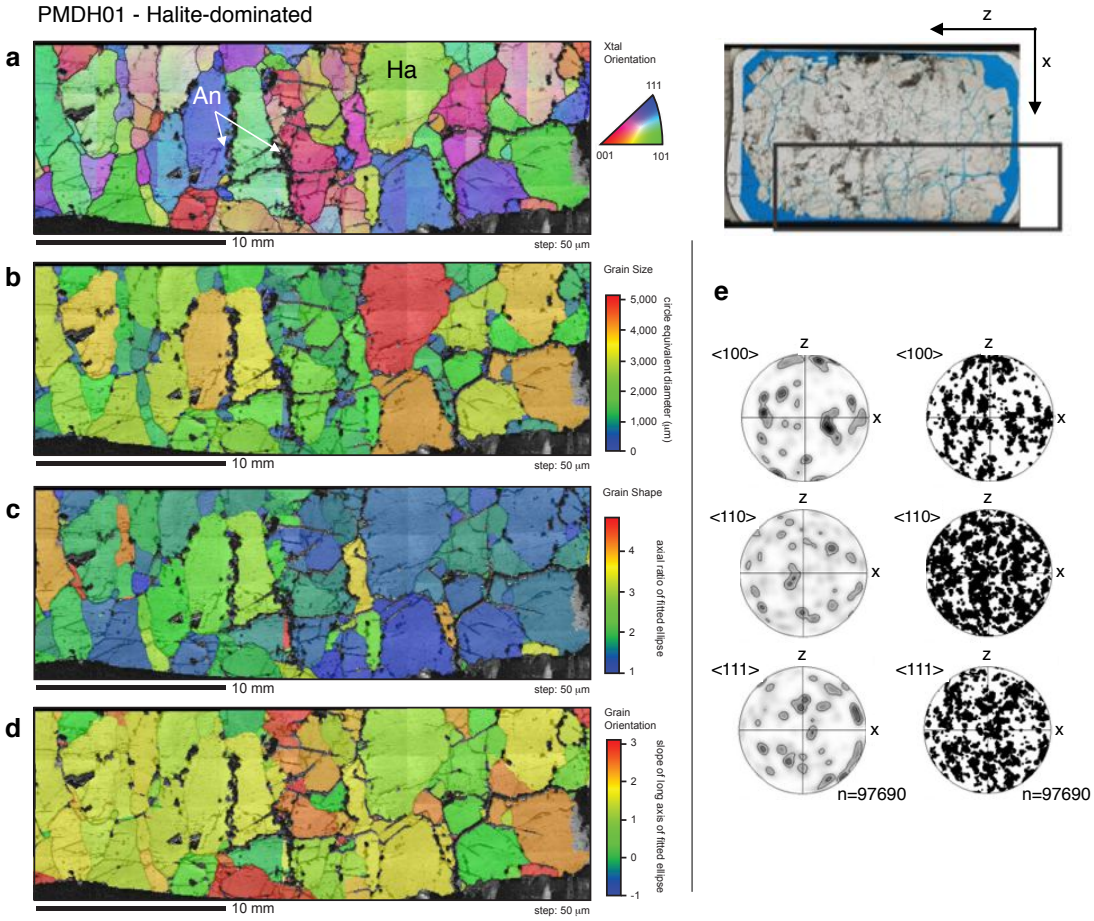

Figure 4: EBSD maps of the halite sample PMDH01. a) Map coloured for crystallographic orientation in Z in the crystal reference frame. b) Map coloured for grain size. c) Map coloured for grain shape. d) Map coloured for trend of grain long axis. Note that maps are composed of several beam scan maps, and that minor orientation artefacts ($<2°$) are present at boundaries individual maps. Grains at the edge of the map can yield false values of grain size, shape and long axis trends. e) {100}{110}{111} pole figures and contoured pole figures of EBSD data from maps on the right hand side; all data points plotted, equal area projection, lower hemispheres. Halite preserved a weak CPO. Contoured plots are multiples of uniform distribution (m.u.d); minimum=0.0, maximum=8.37.

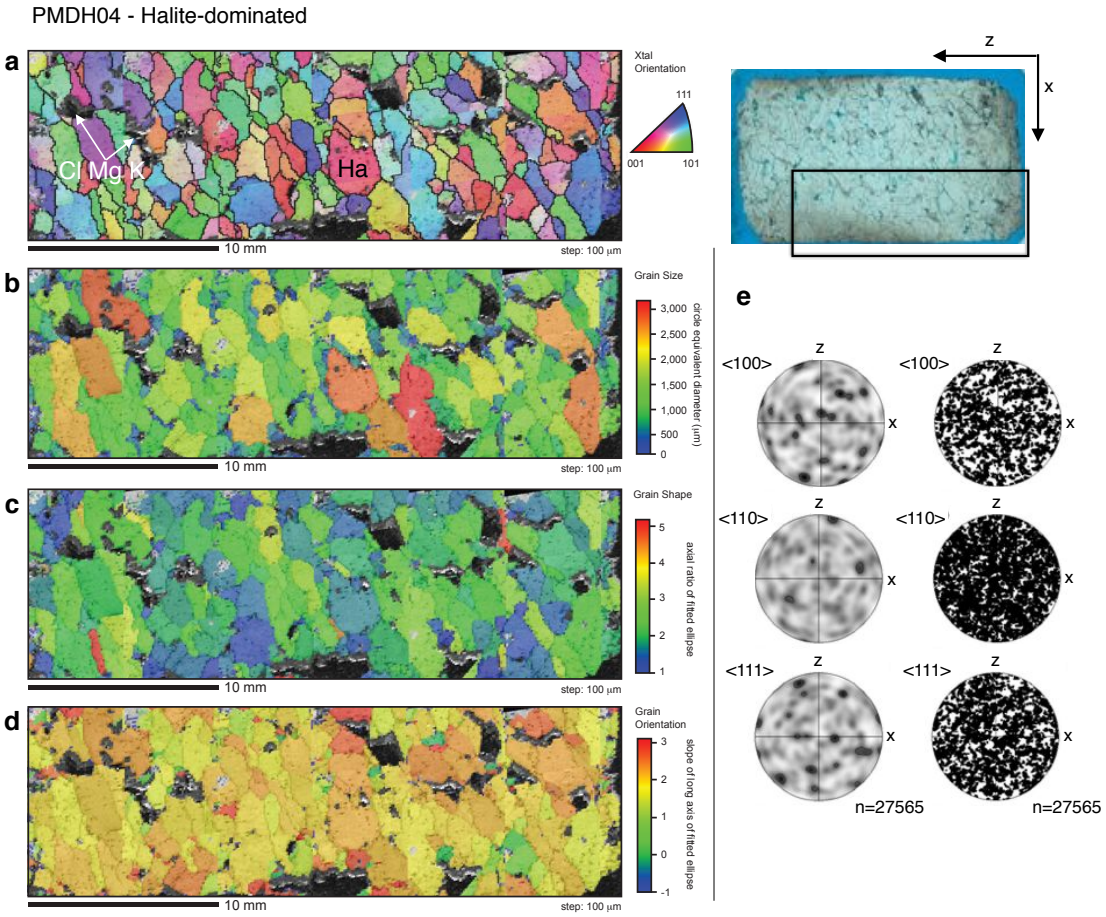

Figure 5: EBSD maps of the halite sample PMDH04. a) Map coloured for crystallographic orientation in z in the crystal reference frame. b) Map coloured for grain size. c) Map coloured for grain shape. d) Map coloured for trend of grain long axis. Note maps are composited from several beam scan maps, and that minor orientation artefacts ($<2°$) are present at boundaries individual maps. Grains at the edge of the map can yield false values of grain size, shape and long axis trends. e) {100}{110}{111} pole figures and contoured pole figures of EBSD data from maps on the right hand side; all data points plotted, equal area projection, lower hemispheres. Halite does not preserved a significant CPO. Contoured plots are m.u.d.; minimum=0.06, maximum=3.11.

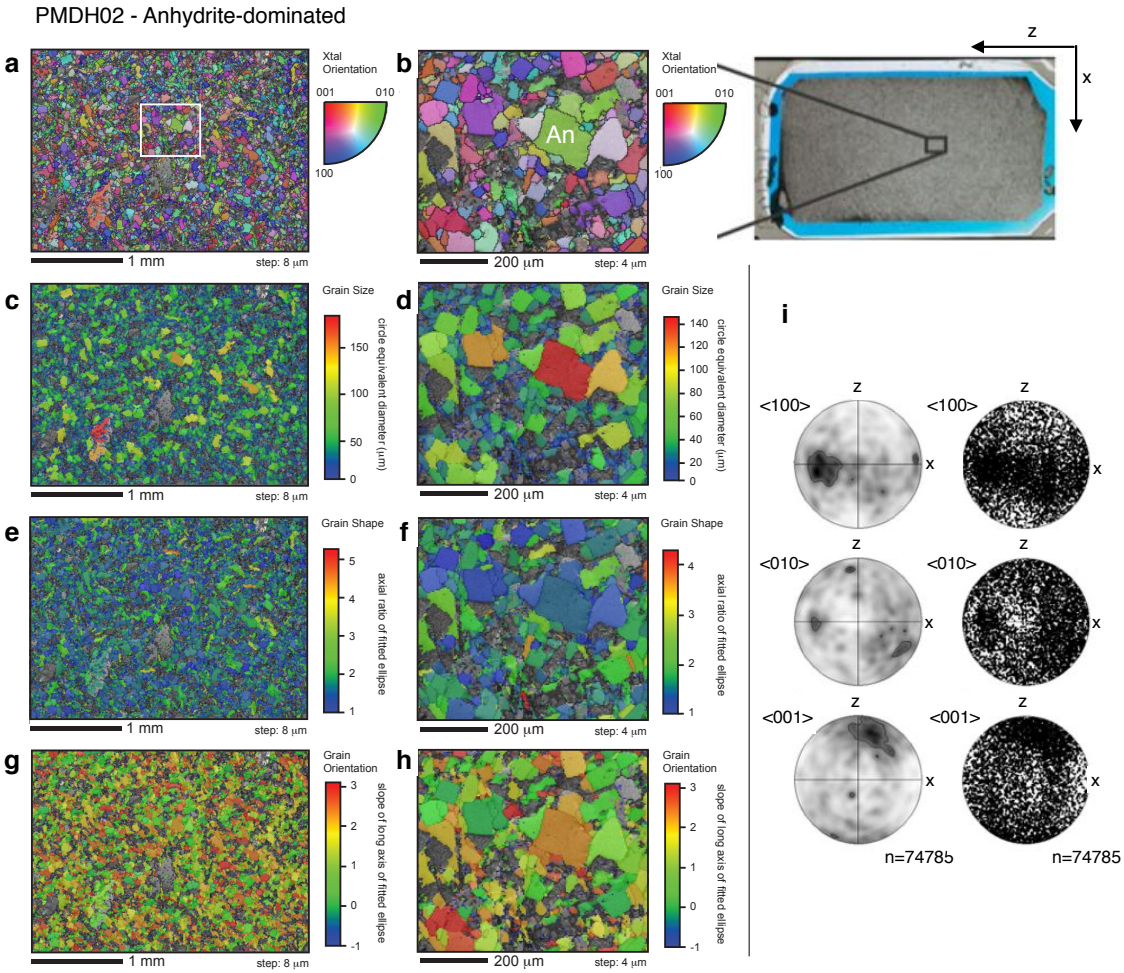

Figure 6: EBSD maps of the anhydrite sample PMDH02. Maps on the right are from inset shown by white rectangle in a). a)-b) Maps coloured for crystallographic orientation in z in the crystal reference frame. c)-d) Maps coloured for grain size. e)-f): Maps coloured for grain shape. g)-h) Maps coloured for trend of grain long axis. i) {100}{010}{001} pole figures and contoured pole figures of EBSD data from maps on the right hand side; all data points plotted, equal area projection, lower hemispheres. Anhydrite preserved a moderate CPO such that poles to {100} are strongly aligned to the foliation and poles to {001} cluster oblique to the foliation plane. Contoured plots are m.u.d.; minimum=0.08, maximum=3.53.

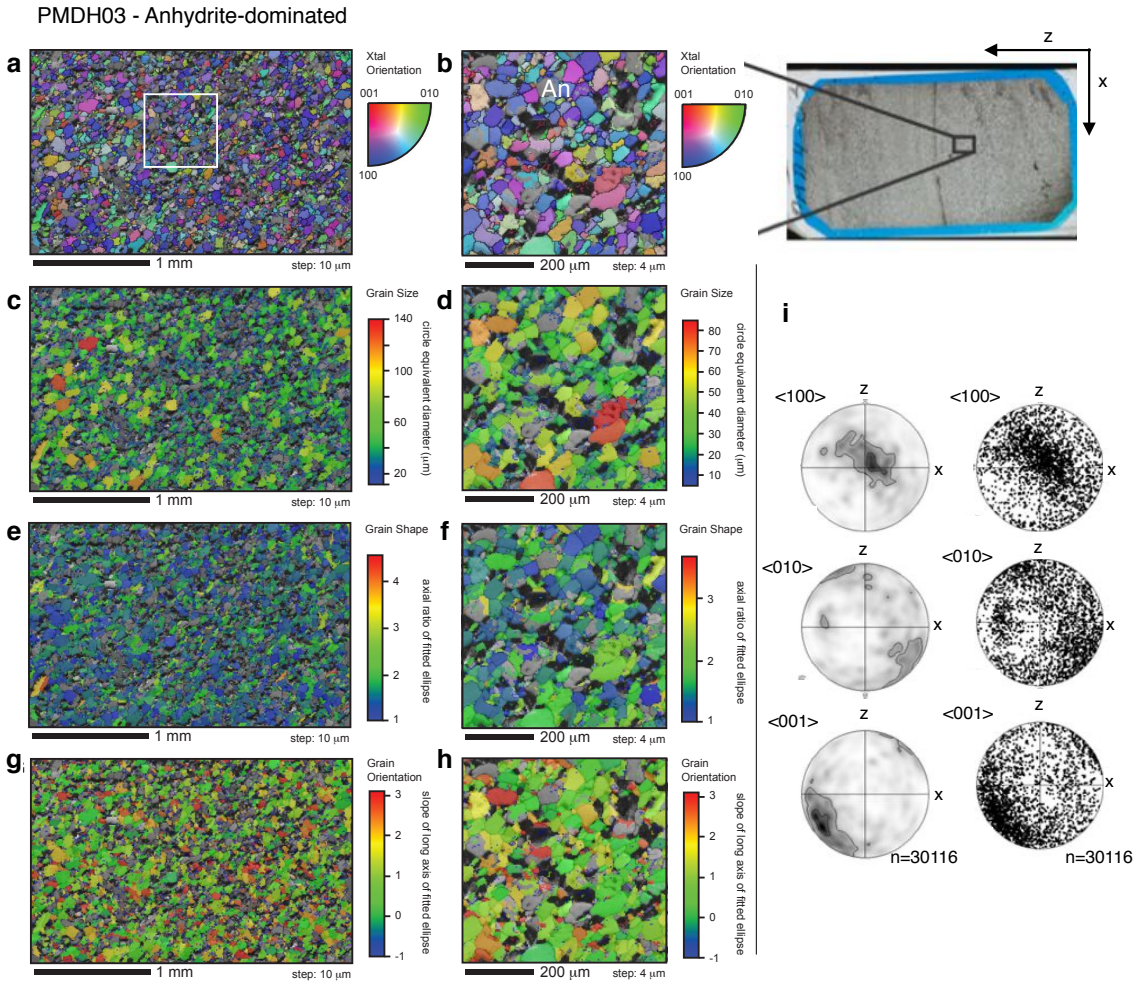

Figure 7: EBSD maps of the anhydrite sample PMDH03. Maps on the right are from inset shown by white rectangle in a). a)-b): Maps coloured for crystallographic orientation in z in the crystal reference frame. c)-d) Maps coloured for grain size. e)-f) Maps coloured for grain shape. g)-h): Maps coloured for trend of grain long axis. i) {100}{010}{001} pole figures and contoured pole figures of EBSD data from maps on the right hand side; all data points plotted, equal area projection, lower hemispheres. Anhydrite preserved a strong CPO, such that poles to {100} are aligned with the foliation plane and poles to {001} cluster oblique to the foliation plane. Contoured plots are m.u.d.; minimum=0.03, maximum=6.44.

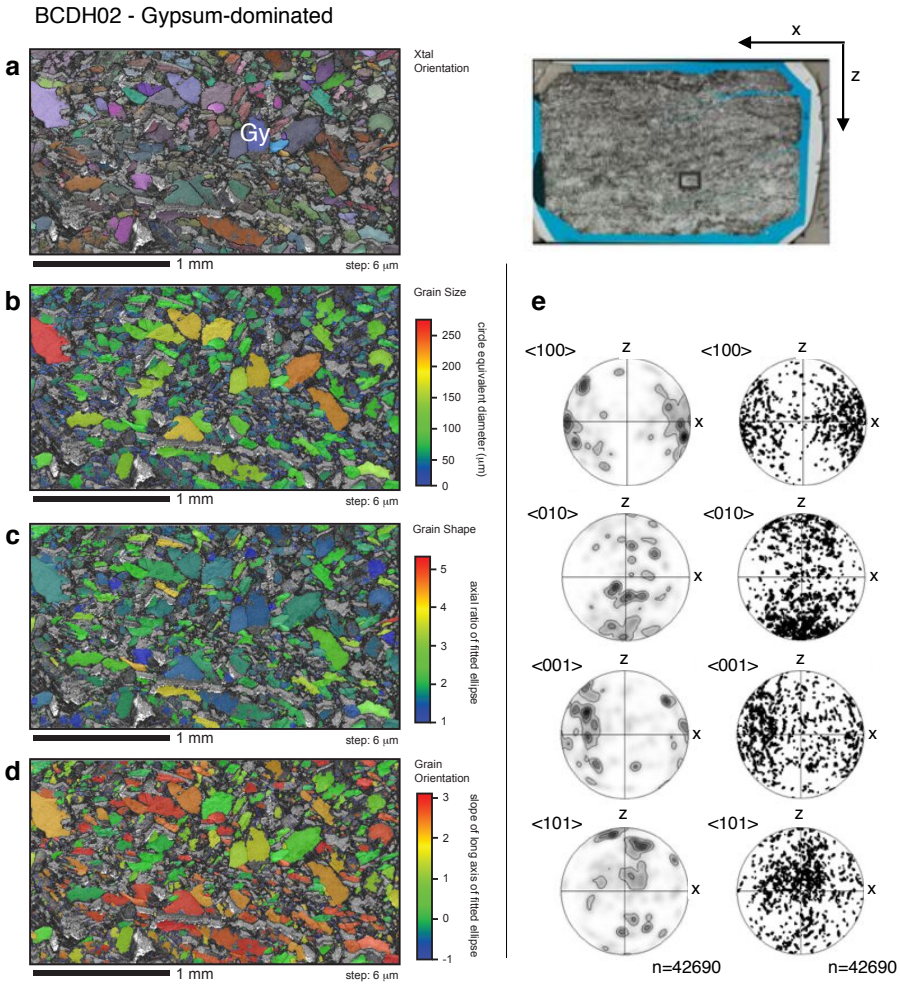

Figure 8: EBSD maps of the gypsum mylonite BCDH02. a) Map coloured for crystallographic orientation by assigning red, blue and green channels to the three Euler angles, respectively. b) Map coloured for grain size. c) Map coloured for grain shape. d) Map coloured for trend of grain long axis. e) {100}{010}{100}{010} pole figures and contoured pole figures of EBSD data from maps on the right hand side; all data points plotted, equal area projection, lower hemispheres. Gypsum shows a strong CPO such that poles to {100} cluster girdle-like parallel to the foliation and poles to {010} cluster perpendicular to the foliation. Contoured plots are m.u.d.; minimum=0.0, maximum=9.75.

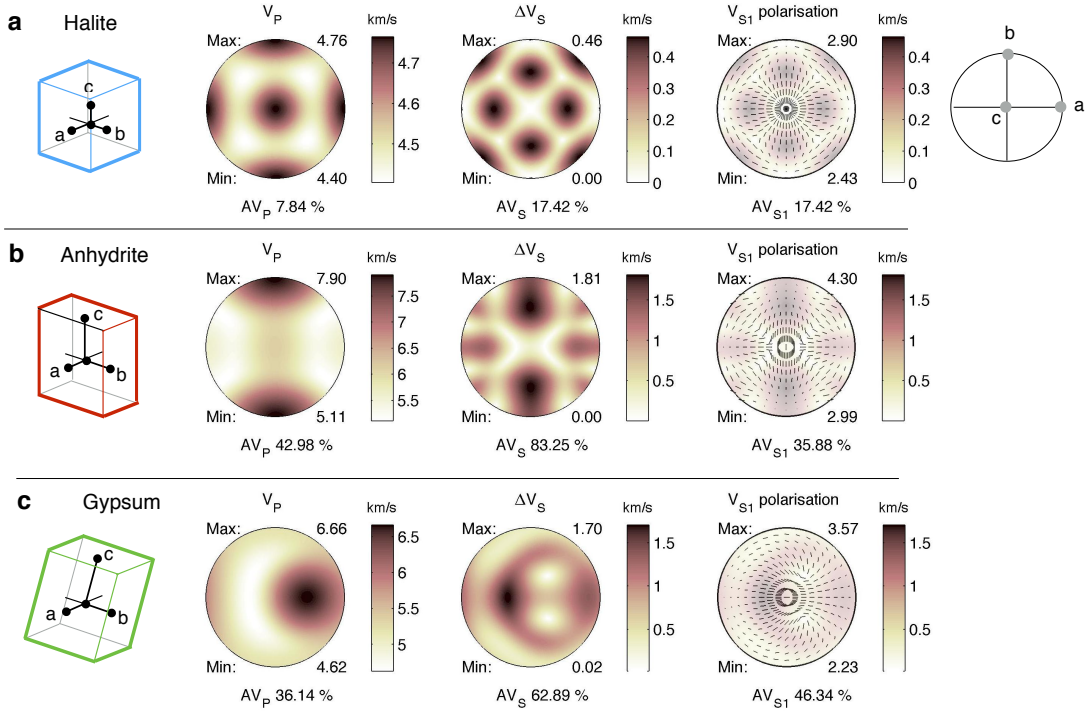

Figure 9: Equal area, upper hemisphere, stereographic projections of compressional velocity (V_P), shear-wave splitting (ΔV_S, Eq. 1) and polarisation of the fast shear wave velocity (V_{S1}) calculated for single crystal of a) halite, b) anhydrite, and c) gypsum relative to the mineral form. Seismic properties were calculated after Mainprice (1990) and appropriate single-crystal elastic properties (Bass, 1995). Note that the velocity distribution clearly reflects the symmetry class of each mineral. Anisotropies are indicated below the projection in percentages, which were calculated with Eqs. 2&3.

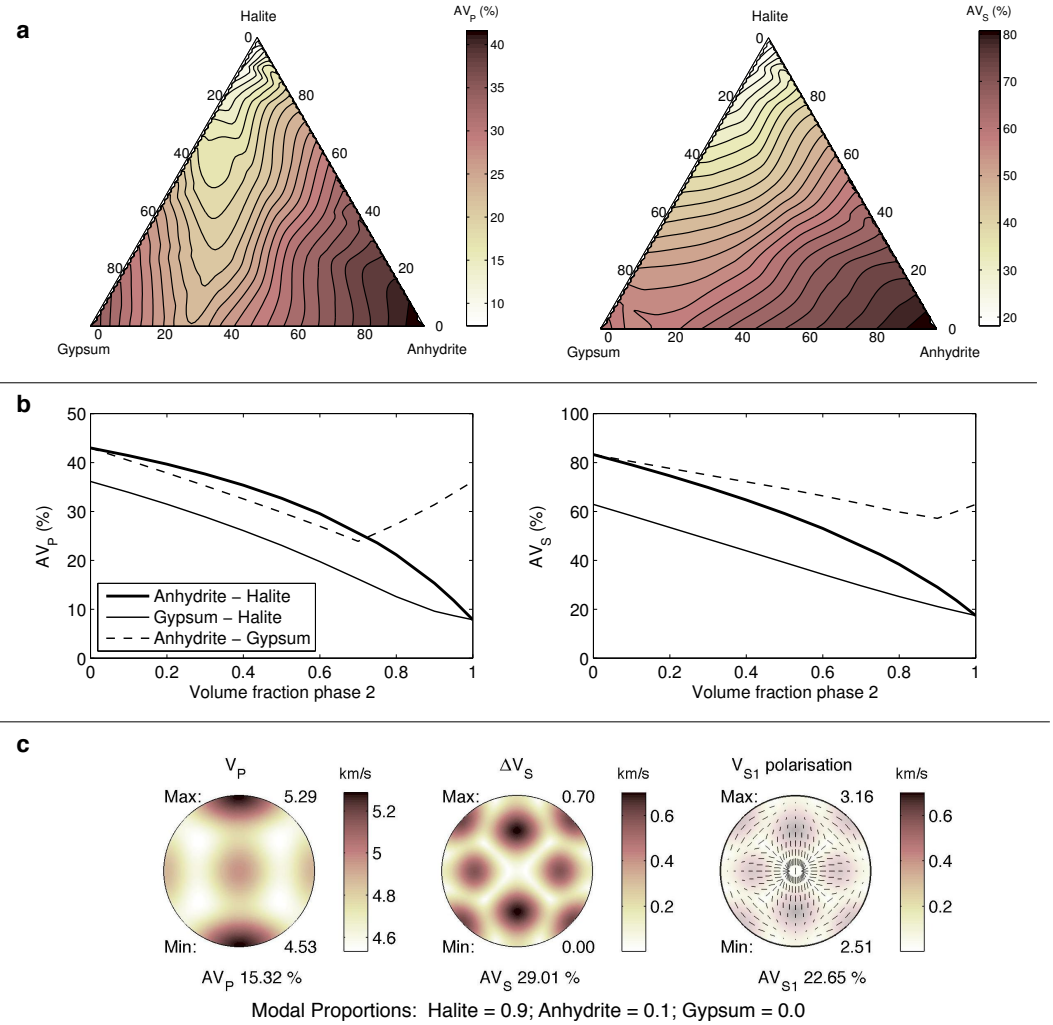

Figure 10: a) Ternary diagrams of the bulk seismic anisotropy AV_P and AV_S predicted by the rock recipe for polycrystalline evaporites consisting of halite, anhydrite and gypsum. Calculations were done after Mainprice (1990) and appropriate single-crystal elastic properties (Bass, 1995). Volume fractions were varied accordingly (after Tatham, 2008), whilst maintaining the CPO regardless the modal content as in c). b) Variation of AV_P and AV_S for two-phase polymineralic evaporites (after Lloyd et al., 2011b). Note the destructive interference between between anhydrite and gypsum and the large increment of anisotropy on a halite-dominated evaporite due to a small volumetric fraction of anhydrite. c) Seismic property distribution for halite-dominated evaporite with 10 % anhydrite content.

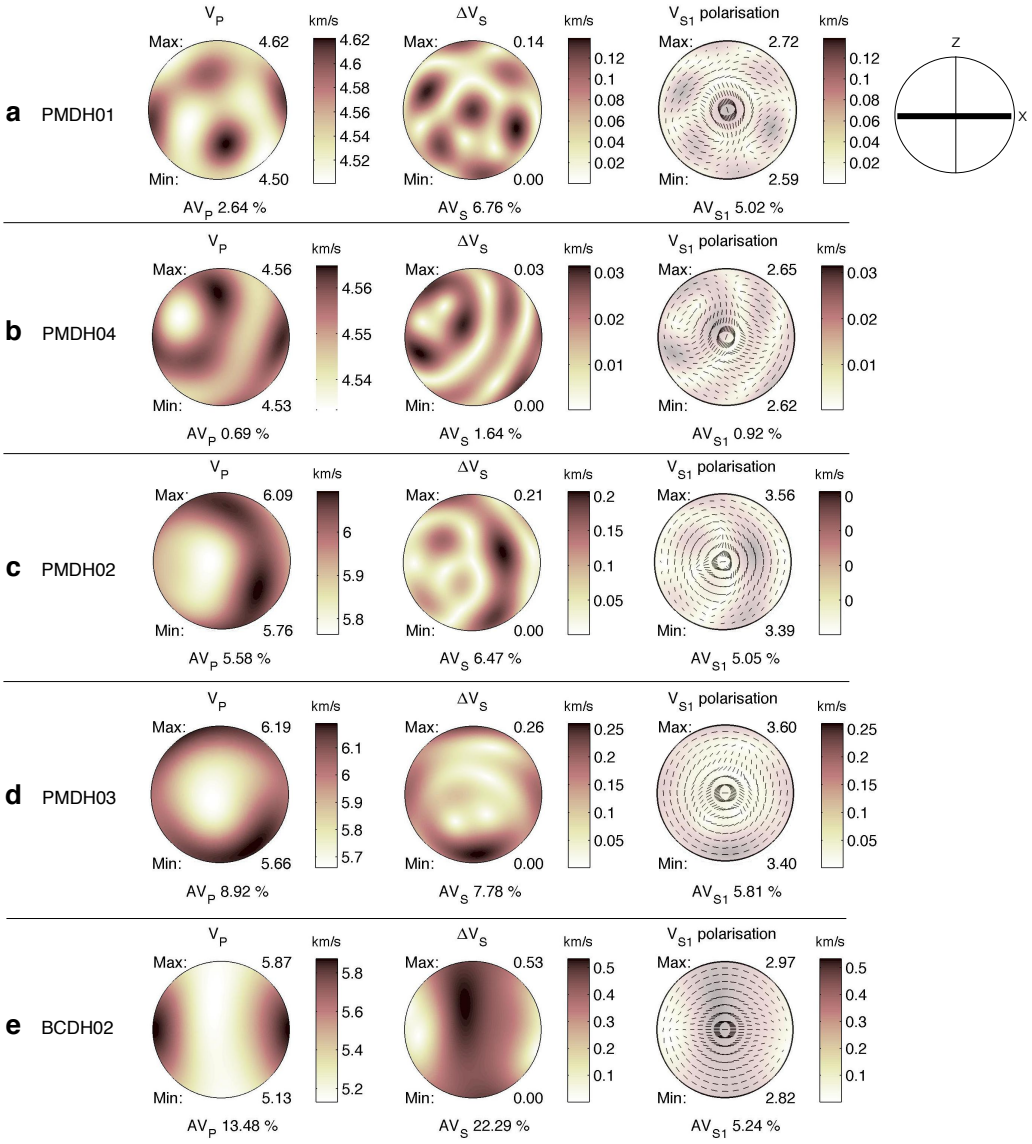

Figure 11: Equal area, upper hemisphere, stereographic projections of compressional velocity (V_P), shear-wave splitting (ΔV_S, Eq. 1) and polarisation of the fast shear wave velocity (V_{S1}) calculated for the indicated samples. EBSD-derived CPO and the stiffness matrix coefficients and densities of single crystals (Bass, 1995) were used for calculations (after Mainprice, 1990). Samples were assumed monomineralic (i.e., volume fraction = 1). Velocity anisotropies AV_P and AV_S (Eqs. 2 & 3) are indicated below the projections as percentage. Properties are projected onto the plane perpendicular to the foliation plane X-Y, indicated by a black horizontal line. Note that the colour scales vary between samples.

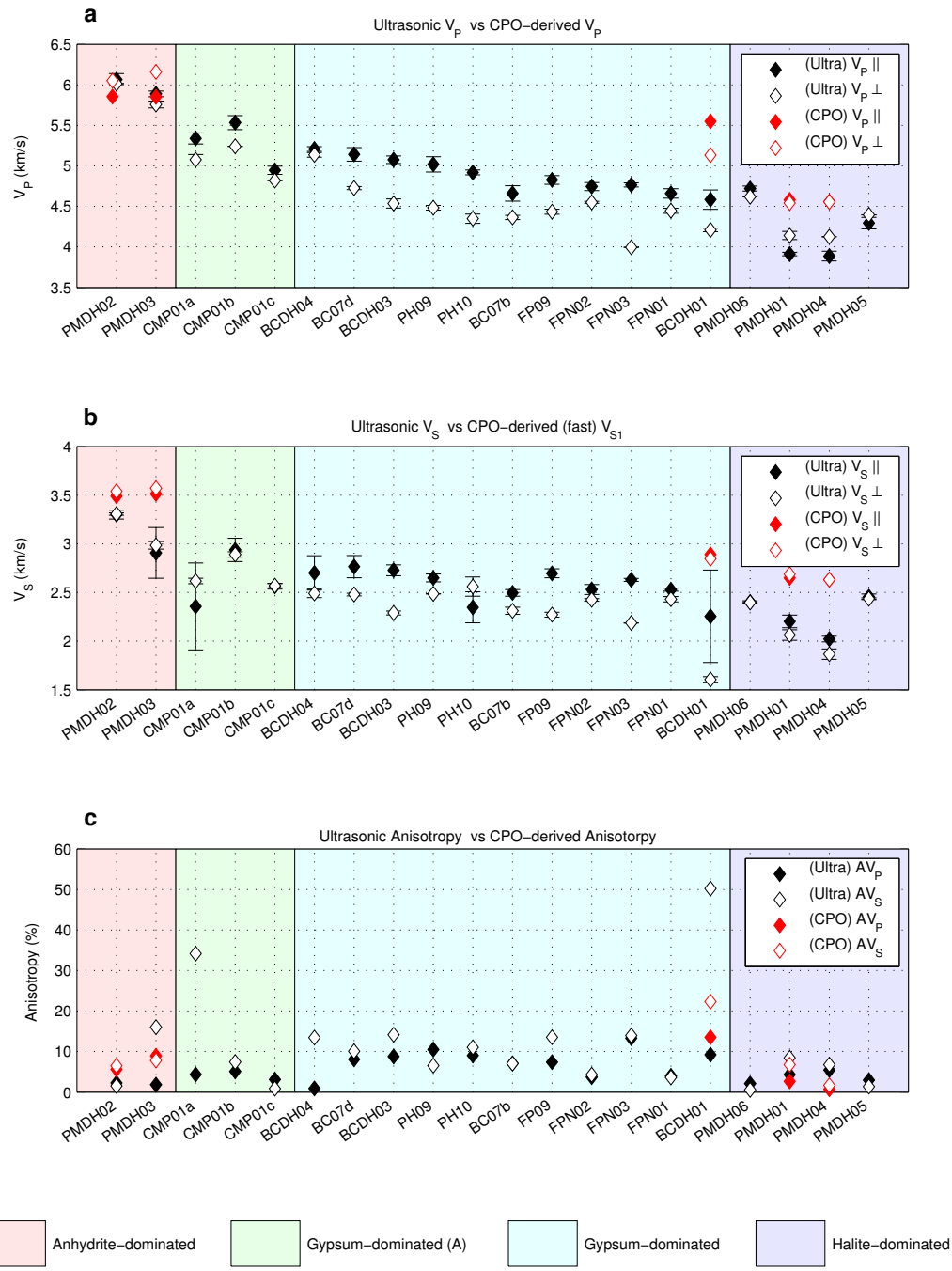

Figure 12: Calculated and measured velocity and anisotropy plots. Velocities indicated as parallel (i.e., parallel to the foliation plane X-Y) are the average of measurements along X and Y directions, where as those indicated as perpendicular are the measurements along the Z-axis (i.e., normal to the foliation plane). Ultra stands for ultrasonic-measured property; CPO stands for CPO-calculated property. Error bars are the standard deviation. In the legend on the bottom, (A) indicates anhydrite content in those samples.